Ramalho, S., Moura, A., Gambaruto, A. M., & Sequeira, A. (2012). Sensitivity to outflow boundary conditions and level of geometry description for a cerebral aneurysm. *International Journal for Numerical Methods in Biomedical Engineering*, *28*(6-7), 697-713. https://doi.org/10.1002/cnm.2461

Sensitivity to outflow boundary conditions and level of geometry description for a cerebral aneurysm

S. Ramalho, A. Moura, A.M. Gambaruto and A. Sequeira

Dept. of Mathematics and CEMAT/IST, Instituto Superior Técnico, Technical University of Lisbon, Av. Rovisco Pais 1, 1049-001 Lisboa, PORTUGAL

SUMMARY

Mathematical models, namely the flow boundary conditions, as well as the detail of the bounding geometry, can highly influence the computed flow field. In this work, an anatomically realistic portion of cerebral vasculature with a saccular aneurysm, and its geometric idealisation, are considered. The importance of the geometric description, namely including the side branches or modelling them as holes in the main vessel, is studied. Several approaches to prescribe the outflow boundary conditions at the side branches are analysed, including the commonly used traction-free condition, zero velocity, meaning that the side branch is neglected, and the coupling with simple 0D models. All these outflow conditions are applied both at the end of the considered 3D side branch, or directly at the junction of the side branch with the main vessel. The 3D side branch is also accounted for by using 1D models. All these effects are compared quantitatively and qualitatively. Results indicate a reduced influence of the fluid boundary condition model when the branches are considered, however the solution is very sensitive in the case of clipped branches. The 0D and 1D models provide good representations of the side branches.

Received . . .

KEY WORDS: Cerebral aneurysm; computational fluid dynamics; outflow boundary conditions; geometrical multiscale.

1. INTRODUCTION

Intracranial aneurysms still represent a frightening and devastating silent threat, not only because they often remain asymptomatic until the time of rupture, but also due to their association with high prevalence and mortality rates [1, 2]. The natural history of this pathology is far from being fully understood. In fact, the intricacy of intracranial aneurysms is reflected on the intensive multi-faceted and multi-disciplinary effort to understand the mechanisms involved in the developmental stages. Inherited and acquired factors may play a role in the aneurysm formation and rupture [3, 4], but specific haemodynamic characteristics, such as wall and oscillatory shear stress, elevated pressure, long cell residence time and flow impingement, are believed to be closely related with the aneurysm initiation and progression [5, 6, 7, 8]. These evidences demonstrate the importance of a detailed comprehension of the local blood flow conditions, which can be useful for both diagnostic and treatment purposes. Thus, even though aneurysm studies are currently based on a variety of methodologies, spanning from *in vitro* [9] to *in vivo* [10] models, a great percentage relies on mathematical modeling and numerical simulations of blood flow in the aneurysm region, using both idealised and patient-specific geometries [8, 11, 12, 13, 14, 15].

Patient-specific geometries can be highly irregular, with sharp curves and a large number of side branches, amongst other factors. Therefore, the prediction of the effect of varying a particular parameter or the choice of the mathematical model becomes more difficult. Thus, even though it has been widely demonstrated that haemodynamics is highly related to the artery and aneurysm geometry, idealised geometries are a valuable tool to independently test the impact of the modelling

choice and the variation of some parameters, at a lower computational cost, while giving a generalisation of the haemodynamics in anatomically realistic models. Prior to performing the simulations on realistic geometries, some researchers use these simplified symmetric geometries as an easier approach to conduct series of validation and optimisation tests, such as to assess the impact of the vessel curvature [15], inclusion of a side branch near the aneurysm [14], incrementation of the angle between parent vessel and aneurysm [13], or even to evaluate the performance of new image reconstruction methods [12]. On the other hand, patient-specific image-based CFD models benefit from being able to realistically reproduce the main haemodynamic features displayed in the aneurysm environment. In fact, the substantial evolution of non-invasive neuro-imaging techniques has allowed for the acquisition and processing of more accurate and detailed medical images, and increasing advances of high performing computers and efficient numerical algorithms lead to even more precise numerical results. Despite the authenticity of the results, a few studies have shown their association with modeling uncertainties, concerning not only variations in the mathematical model but also in the geometrical acquisition and reconstruction [16, 17, 18].

The boundary condition choice may also introduce errors to the solution. In [19] it was demonstrated that the shear stress distribution is sensitive to changes in the inflow parameters, thus, in spite of necessary in some cases, simplifications of the inflow conditions may lead to significant discrepancies between the haemodynamics in the clinical setting and the computed flow field. Realistic inflow conditions, derived from phase-contrast MR imaging measurements in volunteers [8, 12, 20], are a fair approximation, yet the velocity pattern of the patient might be considerably different from the healthy subject. Due to the scarcity of patient-specific flow conditions, many studies make further assumptions using mean flow conditions or typical velocity profiles [16, 21]. In [22] a relationship between flow rates and vessel areas in cerebral arteries was derived in order to allow for the comparison of haemodynamic variables between different cases. Moreover, the acquisition of flow rate measurements for the outflow sections poses a problem, specially when the geometry under study has numerous branches. Many researches work around this by imposing the dependence of the flow division among the downstream sections on the geometry, *i.e.*, prescribing traction free conditions [6, 19, 21]. Imposing a zero stress value at the outflow regions is far from reproducing a physiological situation. For instance, using compliant models with traction-free conditions at outflow causes the appearance of spurious, no physiological, reflections [23]. In order to properly account for the effects of the peripheral circulation and maintain a reasonable computational cost, reduced models, such as 1D and 0D models, can be coupled to the 3D domain in the truncated regions [23, 24, 25, 26, 27]. For example, it is worth mention that the 1D models can act as absorbing boundary conditions, providing the appropriate pressure value at outflow, so that no spurious reflections appear [23]. Although difficult to set up due to their large number of coefficients, the 0D models allow to account for the whole circulation, predicting non intuitive accommodations of the human circulation in pathological cases [27], which otherwise could not be accounted in the numerical simulations.

When using patient-specific image-based CFD models, questions like where to truncate the physical domain or which branches to include, may be raised. The inclusion of insufficient neighbouring side branches may affect the CFD result [10], but the role of small vessels is often neglected [5, 6].

In this work, the haemodynamics inside an aneurysm is studied using the patient-specific and its idealised geometries. The artery is assumed to be rigid and a steady flow regime is considered. A generalised Newtonian fluid model, accounting for the shear thinning behaviour of blood, is applied [16, 23, 26]. The effects of considering or not the presence of side branches closer to the aneurysm are analysed. Different boundary condition approaches at the outflow sections are assessed, including the coupling with reduced models.

2. GEOMETRY RECONSTRUCTION

In this study a CFD analysis is carried out to study the haemodynamics in cerebral aneurysms in a patient-specific geometry and its idealisation.

The patient-specific geometry is reconstructed from medical images obtained *in vivo* from rotational CTA, with resulting voxel resolution of 0.8 mm on a 256^3 grid. The reconstruction procedure of the 3D geometry surface for numerical simulations consists in image segmentation, surface extraction, and finally surface smoothing and meshing. A constant threshold value for segmenting the image data is used, and a marching tetrahedra algorithm is employed to extract the 3D surface that yields the initial triangulation. This approach is fast but assumes that the image intensity of the desired object is sufficiently different from the background to permit a constant threshold choice. It also implies that the medical image resolution is fine enough to perform marching tetrahedra directly, instead of performing an interpolation [29, 30]. Several other segmentation methods exist for image data of cerebral aneurysms, most commonly based on deformable models [6, 31]. However, each method yields a different geometry definition that depends on user defined coefficients and is ultimately limited by the acquisition modality, resolution, contrast and noise.

The resulting virtual model of the vasculature is then prepared for the numerical simulations by identifying the regions of interest and removing secondary branches. Surface smoothing is required due to medical imaging noise and limited resolution that yields an initial surface definition which is not anatomically representative. Smoothing is performed using the bi-Laplacian method, with a final inflation along the local normal by a constant distance, in order to minimise the volume alteration and surface distortion [32]. The intensity of the smoothing is chosen to reduce the surface curvature variation with a constraint that alterations are under the voxel size, which is the basic unit size of uncertainty in interpreting the medical images. Precisely, here the level of smoothing is obtained by means of 200 iterations of the bi-Laplacian method.

Figure 1 shows the initial cerebral arterial geometry, with several secondary branches and a saccular aneurysm, as well as the region of interest that includes the aneurysm and the main side branches, and is used in the numerical simulations.

The idealisation of the patient-specific geometry of Figure 1 is performed using a relevant portion of the main vessel, including the aneurysm, and the thin side branch close to the aneurysm. Thus, the idealisation consists of a tube with constant circular cross-section that is either straight or has a constant radius of curvature. The side branch is represented through a straight tube of constant cross-section, while the saccular aneurysm is represented by a constant radius sphere (see Figure 3). Both the main vessel and the side branch are planar.

These idealisations appear to simplify the anatomically realistic geometry noticeably, maintaining only primitive information. The importance of considering idealised geometries relies in the fact that, being simpler, they provide a clearer understanding of the sensitivity of modelling choice (boundary conditions and level of geometry detail) to the computed flow field. In this work the modelling choice is described by different outflow boundary conditions and by the level of geometry detail that should be included in the region of interest, particularly the inclusion or omission of portions of the side-branches.

In this manner a set of geometry definitions are setup, that can be easily summarised as realistic or idealised geometries, each with portions of the side-branches provided or with holes for the outflows instead.

3. FLUID MODEL AND OUTFLOW BOUNDARY CONDITIONS

Blood is often considered a Newtonian fluid in large to medium vessels (for instance [12, 22, 27, 32]), nevertheless it exhibits non-Newtonian properties, mainly due to the presence and rheological behaviour of red blood cells. In this work the shear-thinning behaviour of blood will be considered, which is one of its main non-Newtonian properties, characterised by the decreasing of the apparent viscosity with increasing shear rate. Given $\Omega \subset \mathbb{R}^3$ the open and bounded domain of interest, and $I =]0, T]$ the time interval, the continuity and momentum equations for incompressible and

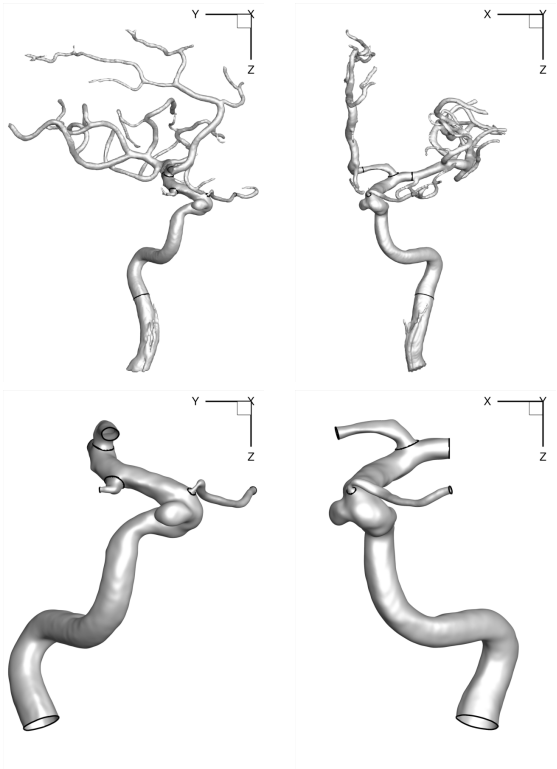

Figure 1. Reconstructed geometry (top row) and detailed view of region of interest (bottom row), showing the different locations where the vessels are clipped. Left column is in the sagittal plane while the right column is in the coronal plane.

isothermal fluids are:

$$\begin{cases} \rho\left(\dfrac{\partial \mathbf{u}}{\partial t} + \mathbf{u}\cdot\nabla\mathbf{u}\right) - \operatorname{div}\boldsymbol{\sigma}(\mathbf{u},P) &= \mathbf{0}, & \text{in } \Omega, \forall t \in I, \\ \operatorname{div}\mathbf{u} &= 0, & \text{in } \Omega, \forall t \in I, \end{cases} \tag{1}$$

where ρ is the density of blood, and $\mathbf{u}$ and P are the unknown velocity and pressure, respectively. The Cauchy stress tensor $\boldsymbol{\sigma}(\mathbf{u}, P)$ is defined through a constitutive law, characterising the rheology of the fluid. A generalised Newtonian fluid will be considered, such that

$$\sigma(\mathbf{u}, P) = -P\mathbf{I} + 2\mu(\dot{\gamma})\mathbf{D}(\mathbf{u}), \tag{2}$$

where $\mathbf{D}$ is the strain rate tensor, given by $\mathbf{D}(\mathbf{u}) = \frac{1}{2}\left(\nabla\mathbf{u} + \nabla\mathbf{u}^T\right)$, and μ is the dynamic viscosity, which is assumed to depend monotonically on the shear rate $\dot{\gamma}$:

$$\dot{\gamma} = \sqrt{\frac{1}{2}\mathbf{D}(\mathbf{u}) : \mathbf{D}(\mathbf{u})}.$$

Different viscosity functions $\mu(\dot{\gamma})$ define different generalised Newtonian models, that can be of shear-thinning, shear-thickening, or yield stress type. Here we consider the Carreau model, for which the viscosity function is given by:

$$\mu(\dot{\gamma}) = \mu_\infty + (\mu_0 - \mu_\infty)\left(1 + (\lambda\dot{\gamma})^2\right)^{\frac{1-n}{2}}, \tag{3}$$

where $\lambda > 0$, and $n, \in \mathbb{R}$ are constants, the coefficients μ_0 and μ_∞ are the asymptotic viscosity values at lower and higher shear rates, respectively. In this case, since the model is shear

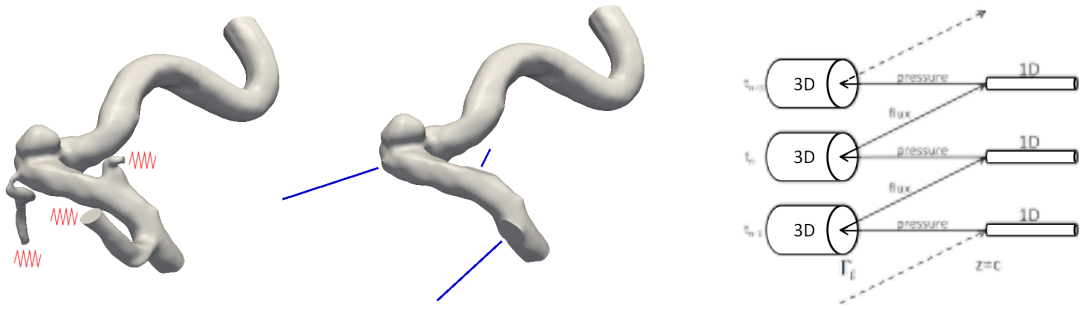

Figure 2. Schematic of the coupling with the 0D model (left) and the 1D model (centre). Scheme of the explicit coupling between the 3D and 1D models (right).

thinning, $\mu_0 > \mu_\infty > 0$. All these parameters are obtained from curve fitting to experimental data. In particular, in this work the parameter values of the viscosity function were estimated from experimental viscosity data obtained by Prof. M.V. Kameneva (Univ. Pittsburgh) for normal human blood (see [16, 23] for details), and are given by $\mu_0 = 0.456Poi$, $\mu_\infty = 0.032Poi$, $\lambda = 10.03s$, e $n = 0.344$.

Equations (1)-(2) are endowed with the initial condition $\mathbf{u} = \mathbf{u}_0$, for $t = 0$, in Ω. The compliance of the artery wall is not accounted for, so that the domain is considered to be rigid and the no-slip condition $\mathbf{u} = \mathbf{0}$ is imposed on the physical boundary. At the inflow section the flow rate, defined according to the section area [22], is prescribed through a parabolic profile. Concerning the outflow artificial sections, general different approaches are studied.

First, the standard traction free, or homogeneous Neumann, boundary conditions are considered in all outflow sections:

$$\sigma(\mathbf{u}, P) \cdot \mathbf{n} = \mathbf{0}, \tag{4}$$

where $\mathbf{n}$ is the outward unit normal to the section. This boundary condition will be always considered at the outflow section of the main vessel, also when other outflow conditions will be applied on the outflow boundaries corresponding to the side branches. Neglecting the side branches will be considered by imposing zero velocity, $\mathbf{u} = \mathbf{0}$, on the side branches outflow boundaries.

Afterwards, the presence of the side branches will be taken into account through reduced 1D or 0D models, by making use of the so called geometrical multiscale approach [25]. It consists of an hierarchical description, where the different parts of the circulatory system are modeled by different dimensional scales coupled together, corresponding to different levels of desired accuracy. Where high levels of detail are necessary, 3D models are used, while to account for the global circulation, reduced 1D or 0D models are coupled to the artificial boundary sections created from the truncation of the 3D domain (see Figure 2).

3.1. The 3D-1D coupling

The 1D model is obtained from the 3D fluid equations (1), by assuming that the artery is a cylindrical compliant tube, with axial symmetry and fixed cylinder axis. The axial velocity is considered to be dominant, pressure is taken constant in each cross section, and the wall displacements are only accounted for on the radial direction. The 1D model is then deduced by integrating in each cross section, assuming a specific axial velocity profile [25]. The result is an hyperbolic system of two equations, corresponding to the reduced form of the continuity and momentum equations:

$$\begin{cases} \dfrac{\partial A}{\partial t} + \dfrac{\partial Q}{\partial z} = 0, \\ \dfrac{\partial Q}{\partial t} + \dfrac{\partial}{\partial z}\left(\dfrac{\alpha Q^2}{A}\right) + \dfrac{A}{\rho}\dfrac{\partial \overline{p}}{\partial z} = -K_r \dfrac{Q}{A}, \end{cases} \quad , z \in (a, b), t \in I, \tag{5}$$

where z is the axial coordinate, $L = b - a$ is the vessel length, and ρ is the constant fluid density. The momentum flux correction coefficient α (see [25] for its definition) is assumed to be constant $\alpha = 1$, corresponding to a flat velocity profile. The friction parameter K_r is defined by $K_r = 8\pi\mu$, where μ is the constant blood dynamic viscosity. Indeed, the 1D model (5) does not account for the shear-thinning behaviour of blood, being obtained from the 3D fluid Newtonian model, with the viscosity μ being the constant Newtonian viscosity. Here, the 1D constant viscosity is considered to be $\mu = 0.04\ Poi$, corresponding to the average experimental viscosity in the range of high shear rates $\dot{\gamma} \in [2, 1000]\ s^{-1}$ (see for instance [11]).

System (5) contains three unknowns, the cross section area $A(t, z)$, the flow rate $Q(t, z)$, and the mean pressure $\overline{p}(t, z)$, and two equations. In order to close the system we assume that the external pressure is zero and consider an algebraic expression relating the blood mean pressure and the area [25, 33]:

$$\overline{p} = \beta \frac{\sqrt{A} - \sqrt{A_0}}{A_0}, \quad \text{where} \quad \beta = \frac{\sqrt{\pi} h_0 E}{1 - \xi^2}, \tag{6}$$

being A_0 and h_0 the cross-section area and wall thickness at rest, respectively, E the Young modulus, and ξ the Poisson ration. Thus, the coefficient β concentrates the mechanical properties of the vessel wall. Both A_0 and β may vary along the vessel length z, however here we consider them to be constant. System (5)-(6) is provided with proper initial and boundary conditions.

The 1D model will be coupled to the 3D rigid model only on the clipped geometries, on the cross sections generated by the crop of the side branches, as illustrated in Figure 2 (middle). Hence, the side branches will be considered as 1D models. Although the 1D system (5) is a compliant model for blood flow in arteries, and the 3D model is rigid, there is no problem regarding pressure waves reflections, since the 1D model is coupled at outflow sections. Moreover, although compliant, it will be seen in the sequel that the 1D model fairly captures the pressure drop of a corresponding 3D rigid tube, since physiological values for the flow rate will be considered. Hence, if the 1D model physical properties, such as cross-sectional area and length, are similar to the ones of the side branches, it provides a good approximation of the pressure drop on the side branch.

The 3D-1D coupling is performed by imposing, at the coupling section interface, the continuity of the flow rate and of the mean pressure [33], noticing that the diffusion term on the 1D momentum equation is a simple friction parameter:

$$-\boldsymbol{\sigma} \cdot \mathbf{n} = p\mathbf{n} - 2\nu \mathbf{D}(\mathbf{u}) \cdot \mathbf{n} = \overline{p}_{1D}\mathbf{n}, \tag{7}$$

$$Q_{3D} = \int_{\Gamma_a^t} \mathbf{u} \cdot \mathbf{n} d\gamma = Q_{1D}. \tag{8}$$

Precisely, the 3D-1D coupling is carried out in an explicit manner, prescribing (8) on the 1D model by computing the flow rate on the 3D outflow coupling section at the previous time, and imposing (7) on the 3D model has a Neumann boundary condition at the current time (see Figure 2 (right)).

3.2. The 3D-0D coupling

Lumped parameters models are derived from the 1D ones by further averaging in space [25, 27], loosing dependence of the spatial coordinate, thus being denoted as 0D models. They consist of a system of ordinary differential equations describing the variations in time of the mean pressure and flow rate in certain compartments of the cardiovascular system, such as the heart, the venous bed, or the pulmonary circulation. For that reason, coupling them with the 3D model allows to account for the global circulation. The 0D models are analogous to electrical networks, the flow rate being identified with the current, the mean pressure with the voltage, the blood viscosity with the resistance, the blood inertia with the inductance, and the wall compliance with the capacitance.

In this study a very simple lumped parameters models of a simple resistance will be used, consisting of an algebraic relation between the flux and the mean pressure through the resistance parameter: $P = RQ$. The resistance parameter R is chosen following [23], as described in the sequel.

The 1D system of equations (5) is hyperbolic and possesses two distinct eigenvalues $\lambda_{1,2} = \overline{u} \pm \sqrt{\frac{\beta}{2\rho A_0}} A^{\frac{1}{4}}$, where $\overline{u} = \frac{Q}{A}$ is the mean velocity. The associated eigenfunctions or characteristic variables are given by

$$W_{1,2}(Q, A) = \overline{u} \pm 4\sqrt{\frac{\beta}{2\rho A_0}} \left(A^{\frac{1}{4}} - A_0^{\frac{1}{4}} \right). \tag{9}$$

Under physiological conditions in haemodynamics, the eigenvalues $\lambda_{1,2}$ have opposite signs, and W_1 and W_2 correspond to the incoming characteristics at the left (inflow) and right (outflow) extremities of the 1D tube, respectively [25]. Notice that $W_{1,2} = 0$ for $A = A_0$ and $Q = 0$, *i.e.*, at rest. Imposing the incoming characteristic on the outflow point W_2 to be zero, corresponds to impose an absorbing boundary condition, since it means there are no waves incoming the domain [23, 33]. From expression (9), imposing $W_2(\bar{p}, Q) = 0$ is equivalent to impose [23]:

$$\sqrt{\frac{8\beta}{\rho A_0}} \left(\bar{p}\frac{A_0}{\beta} + \sqrt{A_0} \right)^2 \left(\sqrt{\bar{p}\frac{A_0}{\beta} + \sqrt{A_0}} - A_0^{1/4} \right) = Q, \tag{10}$$

and performing a linearisation by considering the first order term of a Taylor expansion around zero, the following expression relating the mean pressure and the flow rate is obtained [23]:

$$Q \approx \frac{\sqrt{2} A_0^{5/4}}{\sqrt{\rho\beta}} \bar{p}. \tag{11}$$

This is a good approximation of (10) as long as the Young modulus is sufficiently hight [23]. Namely, it is valid for physiological wall stiffness.

The 0D resistance here considered is the one thus obtained: $R = \frac{\sqrt{2} A_0^{5/4}}{\sqrt{\rho\beta}}$. In a similar manner to the 3D-1D coupling, the 3D-0D coupling is performed explicitly, making use of the flow rate computed from the 3D at the previous time step, to compute the mean pressure at the current time step through (11) and prescribe it as a constant Neumann boundary condition on the 3D coupling interface section:

$$\bar{p}^{(n+1)} \approx \frac{\sqrt{\rho\beta}}{\sqrt{2} A_0^{5/4}} Q^{(n)}.$$

Notice that the resistance parameter thus considered just captures the absorption properties of the 1D model, not corresponding to the equivalent resistance of the 1D tube, since the length is not accounted for. In order to account for the resistance of the 1D tube, the equivalent lumped parameter model, including inductance and compliance, other then the resistance, should be considered. This could be easily carried out (following for instance [26]), but there would not be expected differences between the 3D-1D and the 3D-0D coupling approaches. There are other, more sophisticated 0D models, that might be used [24, 27]. Those are more accurate, but they are also more complex, being very difficult to find the proper lumped parameters, so they will not be addressed here.

4. NUMERICAL SIMULATIONS

4.1. Setup

The simulations were carried out using a patient-specific geometry and the idealisation of its portion including the aneurysm and the closest side branch, as depicted in Figure 2. Geometrical variations were considered regarding only the side-branches, more precisely, including or omitting reconstructed portions of the side branches, for both patient-specific and idealised geometries. This resulted in a total of four different geometries. The four different types of outflow boundary conditions described in Section 3 were considered on the side branches: zero velocity (meaning the side branch is neglected); zero normal stress; coupling with the 0D model; and finally the

coupling with a 1D model of the same length of the side branch (hence only applied in the clipped geometries). As mentioned, in order to make comparisons between each computed solution at the outflow of the main vessel, a zero stress condition (4) was consistently applied.

The numerical solution of the 3D fluid equations (1)-(2) was obtained using the LifeV finite element library (`lifev.org`) with in-house extensions. The discretisation in time was performed by means of a backward Euler scheme. The space discretisation was carried out resorting to $P1-P1$ elements, using streamline diffusion stabilisation [34]. Regarding the 1D model, the Lax-Wendroff scheme was applied for the time discretisation, while P1 finite elements were considered for the space approximation [25]. The Lax-Wendroff scheme is explicit, so a CFL condition must be verified for the 1D model. This results in a smaller time step for the 1D model than for the 3D one. Still, the computational cost of the 3D problem makes it inconvenient to use the 1D time step, thus, two different time steps are considered on the 3D solver, with the 1D model advancing in time with a smaller time step and the same boundary conditions until it reaches synchronisation with the 3D time step.

At each time step a steady state inflow regime is imposed at the inflow section as a parabolic profile. The reference value for the inflow condition was obtained through the relationship between flow rate and vessel areas, derived from measurements in internal carotid and vertebral arteries [22]. The area of the inflow section of the idealised configuration is naturally smaller than the inflow section of the patient-specific geometry, since it lies downstream. However, for comparison purposes and since no side branches are considered before the inflow section of the idealised geometry, the same flow rate is prescribed in both geometries. Thus, given the relation $Q = k \cdot A^n$ with the constants $k = 48.21$, and $n = 1.84$ (see [22]), and the area of the inflow section of the anatomically realistic geometry, $A = 0.208\ cm^2$, the prescribed inflow steady flux is $Q = 2.67\ cm^3 s^{-1}$. The inflow flux is ramped up from the initial rest state $Q = 0\ cm^3 s^{-1}$, using $Q_{in}^{ramp}(t) = \frac{t\,Q}{t_{ramp}}$, for $t < t_{ramp}$, with the time length of the ramp chosen to be $t_{ramp} = 0.01\ s$. The computations were run until steady state was reached, identified by negligible differences, O(10^{-10}), in the solution. In all cases, the simulations were carried out using a time step of $10^{-3}\ s$ on the 3D model, while a time step of $0.5 \times 10^{-4}\ s$ was taken for the 1D model.

Concerning the 1D hyperbolic model, an absorbing boundary condition, $W_2 = 0$, was considered at the downstream section of the 1D tube. For both 1D and 0D models, the β parameters used were determined through equation (6), where the thickness of the wall h_0 was set to be 10% of the vessel radius, the Young Modulus $E = 10^5\ dyn/cm^2$, and the Poisson ratio is set to $\xi = 0.5$, assuming that the artery wall is incompressible. As described in Section 3, the coupling of the 3D fluid model with the reduced 1D and 0D models is performed by means of an explicit algorithm, and the defective mean pressure data provided by the reduced model is imposed on the outflow section of the 3D model through a Neumann boundary condition (see [33] and references therein regarding defective boundary data).

The simulations considering the patient-specific geometry with the side branches were executed using a graded mesh with element size of $0.02\ cm$ within the aneurysm, and maximum size of $0.05\ cm$, amounting to using around $1.9\ M$ tetrahedral elements. Regarding the clipped patient-specific geometry, a finite element mesh of about $1.2\ M$ tetrahedra was employed, corresponding to a maximum element size of $0.04\ cm$. Concerning the idealised configurations, both branched and clipped geometries meshes were composed of approximately tetrahedral $1.1\ M$ elements, corresponding to a maximum size of $0.04\ cm$.

4.2. Discussion

The results were obtained considering the entire geometry unless explicitly stated. The specific cases where selected regions of the geometries are considered relate primarily to cross-sections of the flow field or flow within the aneurysm. The following abbreviations of the boundary conditions applied are used in the figures and tables: TF for traction free conditions, V0 for no-slip velocity, 0D for the 0D resistance model, 1D when using the 1D model. Furthermore the subscripts (cl) and (br) are used to indicate if the geometry is clipped or has branches, respectively. For example, $_{\text{br}}$0D

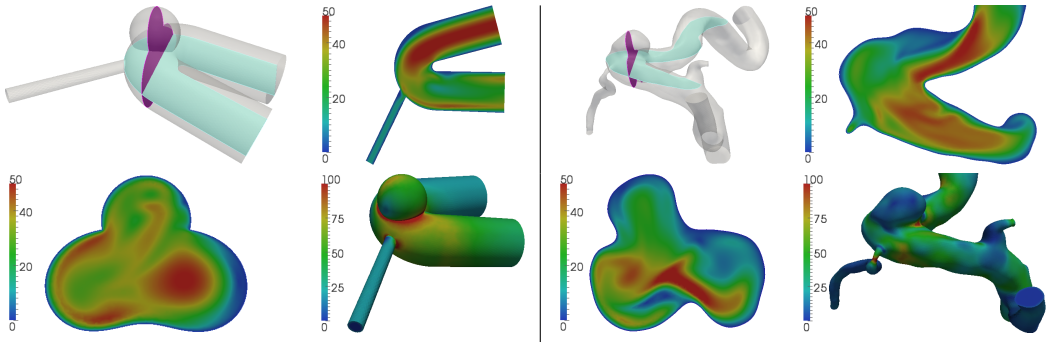

Figure 3. Geometries including the side-branches coupled with a 0D model ($_{br}$0D). Illustration of the chosen cross-sections (top-left), velocity magnitude (cm/s) in both cross-section (top-right and bottom-left), and WSS magnitude (dyn/cm^2) (bottom-right). Note that the velocity cross-section that includes the aneurysm is such that the upstream flow is on the right and downstream on the left.

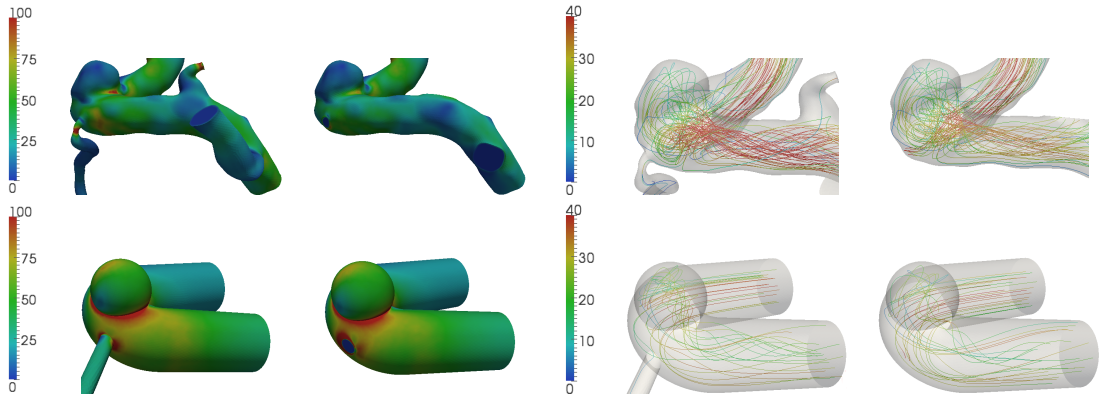

Figure 4. Distribution of WSS magnitude (dyn/cm^2) and velocity pathlines (coloured be velocity magnitude) between the geometry with and without side branches, using the TF boundary condition, hence $_{cl}$TF and $_{br}$TF.

indicates that the geometry includes side branches to which the 0D model is coupled, as shown in Figure 3, where locations of the cross-sections are also illustrated.

In Figure 3 velocity cross-sections and WSS distributions are shown for $_{br}$0D, while in Figure 4 the WSS distribution and velocity pathlines for $_{br}$TF and $_{cl}$TF are shown, for both the idealised and realistic geometries. Clear differences are visible and, importantly, we observe that within the aneurysm the realistic geometry has lower WSS and velocity than its idealisation. Downstream of the aneurysm, the velocity magnitude decreases abruptly in the idealised geometry, contrary to the realistic one. The large differences seen are likely due to the simplified inflow velocity profile, as well as the reduction of the vessels to have constant diameter and the main vessel also a constant radius of curvature at the bend, on the idealised configuration. The local change in vessel surface for the realistic geometry allows for more complicated and small scale flow features to be present, as shown by the velocity cross-sections and velocity pathlines, reducing the formation of larger flow structures and resulting in a reduced WSS. Despite these differences, however, some features between the realistic and its idealisation are comparable such as the flow split in the first side branch which are 2% and 1% respectively for $_{br}$0D, and 2% and 3% for $_{br}$TF, while greater differences are seen for $_{cl}$TF, as shown in Table I.

In Table I the pressure drop values between the inflow and the first side branch are also presented, as well as between the inflow and the outflow of the main vessel. The pressure drops for the different cases studied help in giving insight into the obtained solutions and the boundary condition choice. At first glance it is apparent that the traction-free boundary condition is almost equivalent to impose

a pressure, giving approximately the same pressure drop between inflow and the side-branch and main vessel outflows. The traction-free boundary condition hence assumes that the pressure at all outlets is approximately the same; physically this is equivalent to assuming that the same level of the cardiovascular tree is reached at these outflow sections, which is not physiological. For the idealised geometry the pressure drop to the main vessel outflow remains relatively constant with variation of outflow boundary conditions, while that at the side-branch changes significantly, resulting in a substantial flow split difference. For the anatomically realistic geometry a greater difference is seen in pressure drops in general, however the 0D and 1D models respond similarly. The no-slip condition causes a greater pressure drop to the main vessel outflow due to the increased flux throughout the vessel. In the clipped case of the realistic geometry, the traction-free boundary condition causes a large flux to exit the side-branch while the 0D and 1D give a better representation. However, it is important to note that the no-slip boundary condition on the clipped realistic geometry yields a flow split closer to the realistic geometry with branches, due to the high flow resistance of the first side-branch.

		TF	V0	0D	1D
Idealised	Clipped	1054 / 8%	−263 / 0%	9 / 3%	−32 / 3%
		1095 / 92%	1163 / 100%	1134 / 97%	1136 / 97%
	With branch	1129 / 2%	−390 / 0%	624 / 1%	
		1143 / 98%	1160 / 100%	1149 / 99%	
Real	Clipped	2612 / 16%	1581 / 0%	1846 / 8%	2193 / 12%
		2609 / 38%	4000 / 100%	3176 / 66%	3020 / 60%
	With branch	3616 / 3%	1573 / 0%	3411 / 2%	
		3620 / 83%	4059 / 100%	3802 / 90%	

Table I. Flow rate division (right, percentage with respect to the inflow flux) and pressure drop (left, dyn/cm^2), for different geometries. For each case the first row presents these results between the inflow section and the end of the first side branch, while the second row relates the inflow and the outflow section of the main vessel.

The several differences in the computed solutions preclude a direct qualitative analysis, so that the realistic and idealised geometries will be compared qualitatively. The idealisation serves as an approximate solution to the realistic case, with the advantage that the simplified form will emphasise the effects of varying the outflow boundary condition to the first side-branch. This is due to representative flow field in the idealised geometry, with reduced presence of complex secondary flows.

The remainder results presented are focused on the differences in the computed solutions. The selective comparisons made are based on the perspective of an end user who wishes to perform numerical simulations of haemodynamics in large arteries with physiological relevance. Thus, the effects of different branch outflow boundary conditions are compared to the traction-free boundary condition, as this is the most commonly used in the literature.

As a first comparison, the reference geometry is the clipped case. Selected results are presented in Figures 5, 6, 7. The values of differences in velocity and WSS magnitude are presented in Table II. From the velocity cross-sections (Figures 6, 7) and WSS map (Figure 5), it is apparent that the $_{cl}$1D-$_{cl}$0D comparison presents small differences in the flow field, as expected, while $_{cl}$TF-$_{cl}$V0 presents the greatest difference both in the vessel and aneurysm. These results are common to both the realistic and idealised geometries, however a noticeable difference appears in $_{cl}$1D-$_{cl}$0D for the realistic geometry. In order to clarify this difference it is noteworthy to remember that the 0D model corresponds to imposing a zero incoming characteristic of the 1D model directly at the interface section, so that its resistance represents the absorption of the corresponding 1D wave. However, as already mentioned in Section 3.2, it does not coincide with the resistance of the 1D tube, nor take into account its length.

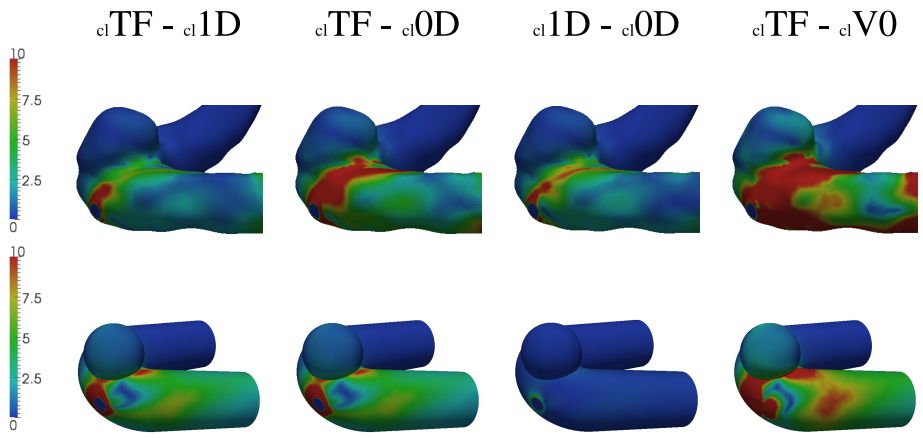

Figure 5. Differences of the WSS magnitude (dyn/cm^2) between different boundary conditions using the geometry without side branches.

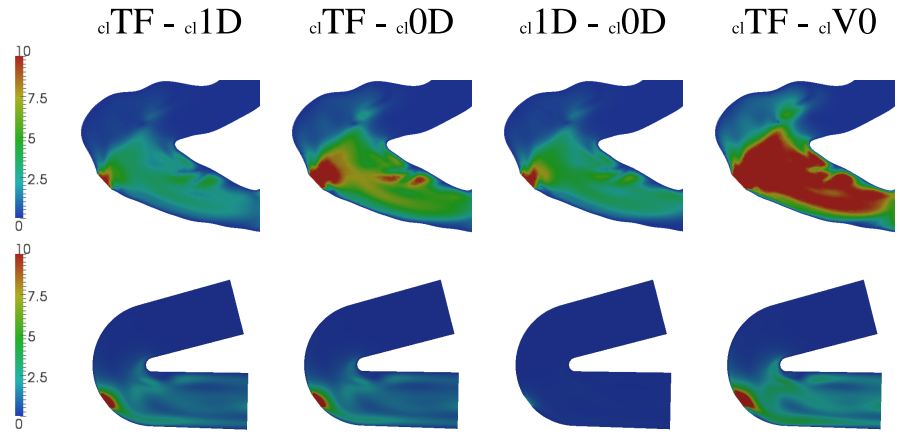

Figure 6. Differences of the velocity magnitude (cm/s) between different boundary conditions using the geometry without side branches (planar cross-section).

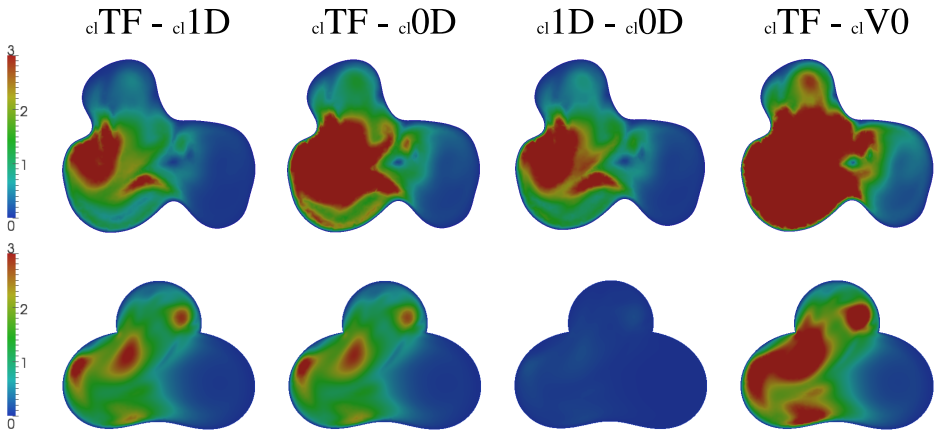

Figure 7. Differences of the velocity magnitude (cm/s) between different boundary conditions using the geometry without side branches (transverse cross-section).

As a second comparison, a portion of the reconstructed side-branches are included and a traction-free boundary condition is imposed (brTF), and a comparison of this computed flow field to the

	test case	Max diff Velocity	Mean diff Velocity	Max diff WSS	Mean diff WSS
Idealised	clTF - cl1D	35 (141%)	0.544	146 (99%)	0.005
	clTF - cl0D	33 (133%)	0.513	139 (95%)	0.005
	cl1D - cl0D	2 (9%)	0.03	7 (5%)	0.0003
	clTF - clV0	63 (251%)	0.845	236 (161%)	0.008
Realistic	clTF - cl1D	12 (49%)	0.791	29 (20%)	0.012
	clTF - cl0D	27 (107%)	1.177	43 (29%)	0.018
	cl1D - cl0D	15 (60%)	0.386	23 (16%)	0.005
	clTF - clV0	55 (221%)	2.579	79 (54%)	0.038

Table II. Comparison between different boundary conditions using a clipped geometry. The maximum difference for the velocity is calculated for the planar cross-section, using the maximum inflow value for the percentage. The maximum difference for the WSS is for the whole geometry.

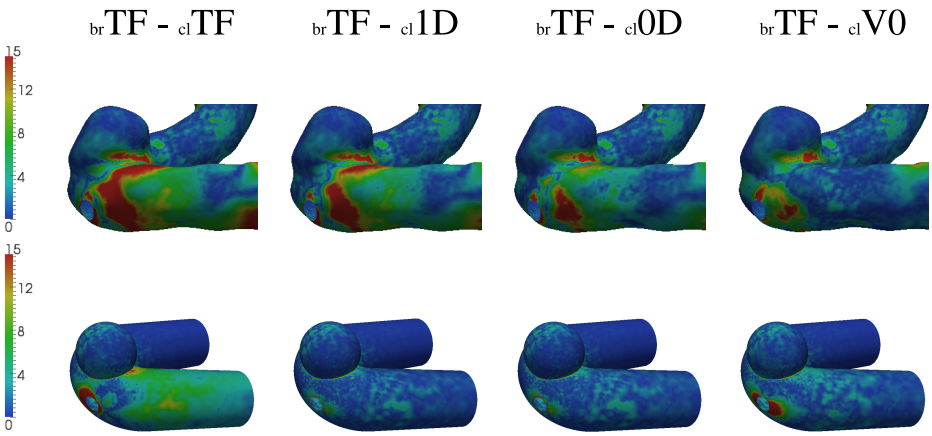

Figure 8. Differences of the WSS magnitude (dyn/cm^2) between the geometry with and without side branches.

different outflow conditions in the clipped geometry is undertaken. Selected results are displayed in Figures 8, 9, 10, while the respective differences are presented in Table III. From the velocity cross-sections (Figures 9, 10) and WSS map (Figure 8), the brTF-cl1D and brTF-cl0D highlight the smallest differences in the flow field for the idealised configuration, while brTF-clTF has the greatest differences in both geometries. This is also mirrored in the flow division as shown in Table I.

When considering the realistic geometry, the influence of the different boundary conditions is not readily carried through from the idealised case, unlike when comparing the boundary conditions for the clipped geometry. The principal reasons for this is the complex shape of the side-branches and their tapering. For instance, the idealisation of the side-branch is simplistic since it does not take into account its irregularities, not only in terms of area variations but also due to the sharp bends. Hence, while the 1D tube model parameters, such as constant radius and length, correspond to the side-branch of the idealised geometry, that is not the case for the realistic one. In the case of the 1D and 0D models, the boundary conditions applied to the clipped geometry depend locally on the area of the side-branch, and do not take into account the drastic reduction of the side branches area. Furthermore, the shape of the side-branches is not considered in the 1D and 0D models, namely curvature and non planarity. This results in large discrepancies when comparing brTF to cl1D and cl0D. In the case of the brTF-clV0 comparison, the differences are relatively small due to the stenosis in the first side-branch that greatly reduces the flow in it. That is also confirmed by the flow division, that, for the realistic configuration in the first side branch, is 3% in the case brTF, and 0%, 8% and 12% in the cases clV0, cl0D and cl1D, respectively, as displayed in Table I.

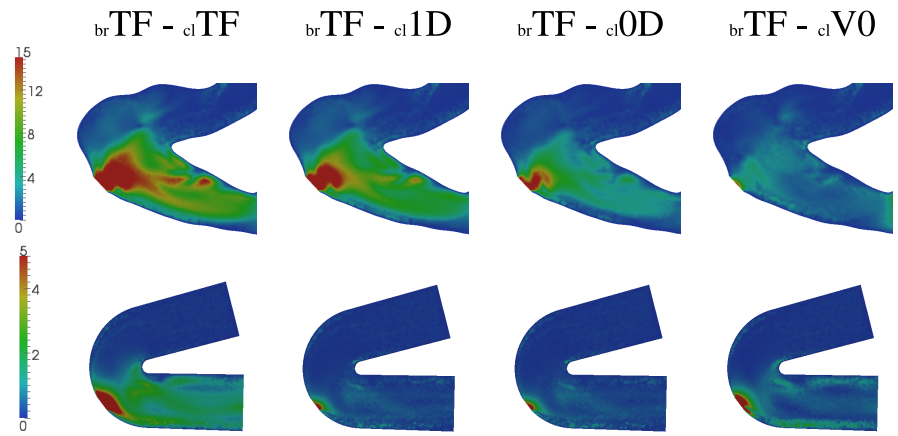

Figure 9. Differences of the velocity magnitude (cm/s) between the geometry with and without side branches (planar cross-section).

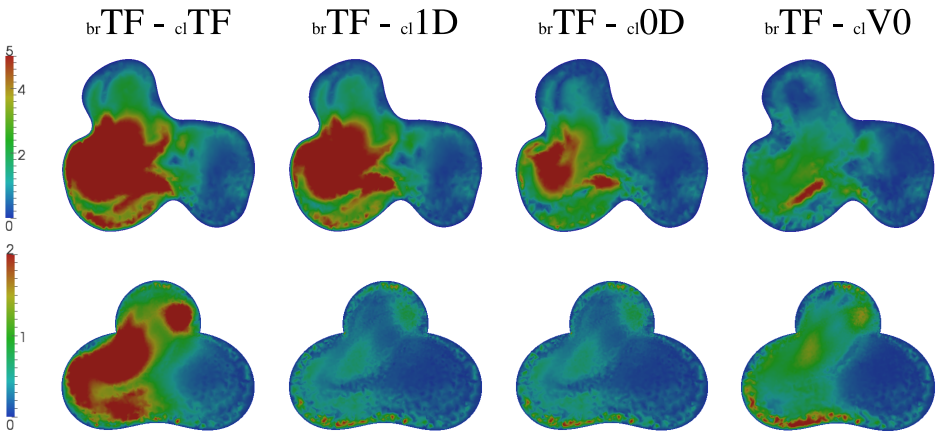

Figure 10. Differences of the velocity magnitude (cm/s) between the geometry with and without side branches (transverse cross-section).

	test case	Max diff Velocity	Mean diff Velocity	Max diff WSS	Mean diff WSS
Idealised	brTF - clTF	57 (229%)	0.528	206 (140%)	1.95
	brTF - cl1D	29 (115%)	0.016	61 (42%)	0.71
	brTF - cl0D	31 (123%)	0.014	68 (46%)	0.76
	brTF - clV0	30 (121%)	0.32	78 (53%)	0.98
Realistic	brTF - clTF	48 (191%)	1.904	61 (41%)	6.23
	brTF - cl1D	38 (151%)	1.113	51 (34%)	4.29
	brTF - cl0D	25 (99%)	0.727	46 (31%)	3.39
	brTF - clV0	14 (57%)	0.675	44 (30%)	3.05

Table III. Comparison between different boundary conditions using a geometry with and without side branches. The maximum difference for the velocity is calculated for the planar cross-section, using the maximum inflow value for the percentage. The maximum difference for the WSS is for the whole geometry.

It is therefore difficult to infer a more appropriate boundary condition model for the outflow sections. It is also apparent that the traction-free boundary condition is not a good representation in

the clipped geometry, and considering it is non-physiological in the branch geometry, as it assumes approximately equal pressure, so it should be used with care.

5. CONCLUSIONS

In this work an anatomically realistic geometry of a cerebral aneurysm and its idealisation were considered to study the importance of outflow boundary conditions. This was performed at two levels: firstly considering the geometric detail of the side-branches, using either the reconstructed surface or clipping these to leave only holes in the main vessel; and secondly by considering a set of four different outflow boundary condition models: traction-free (TF), zero velocity (V0), coupling with a 0D resistance (0D), and coupling with a 1D model (1D) with the side branch length. The latter was enforced only on the geometry where the side branches were not included, substituting the side branch

The idealisation of the geometry was useful since the complexity of the flow field was reduced. It therefore allowed for a better understanding of the influence of the side branches as well as the different outflow boundary conditions applied. In particular, the reduced models seemed promising in accounting for the side branches, providing a faired pressure drop at the branch outflow sections. However, the anatomically realistic geometry is required in order to include the appropriate level of detail. While results for these two geometries are comparable, no direct conclusion from the idealised geometry can be inferred for a patient-specific study.

When modelling the 3D side branch using several boundary condition approaches, the TF or OD models provide similar results. When comparing the results including the 3D side branch with those using the clipped geometry, the 0D and 1D models yield the closest solutions to the 3D branch. Nevertheless, these reduced models do not take into account the change in cross-sectional area nor the tortuous shape of the side-branches.

As main conclusion, the 0D and 1D models seem to be the more appropriate outflow boundary conditions, however it is necessary to study a larger number of geometries. Also, the lack of clinical data for flow velocity at different locations of the vascular network makes it difficult to assess the accuracy rigorously.

Nevertheless, the results in this work demonstrate that in both cases of realistic and idealised geometries, the prescription of outflow conditions is very important, highly influencing the haemodynamics inside the aneurysm, and they should be chosen with special caution.

ACKNOWLEDGEMENT

We greatly acknowledge Prof. Jorge Campos, and his team from the Faculty of Medicine of the University of Lisbon, for providing us the *in vivo* rotational CTA scans of specific patients. This work has been partially funded by FCT (Fundação para a Ciência e Tecnologia, Portugal) through grants SFRH/BPD/34273/2006 and SFRH/BPD/44478/2008, and through the project UTAustin/CA/0047/2008.

REFERENCES

1. Krex D, Schackert HK, Schackert G. *Genesis of cerebral aneurysms - an update*. Acta Neurochirurgica, 143(5):429-49, 2001.
2. Rinkel GJE, Djibuti M, Algra A, Van Gijn J. *Prevalence and risk of rupture of intracranial aneurysms: a systematic review*. Stroke, 29(1):251-56, 1998.
3. Onda H, Kasuya H, Yoneyama T, Takakura K, Hori T, Takeda J, Nakajima T, Inoue I. *Genomewide-linkage and haplotype-association studies map intracranial aneurysm to chromosome 7q11*. The American Journal of Human Genetics, 69(4):804-19, 2001.
4. Pope FM, Narcisi P, Neil-Dwyer G, Nicholls AC, Bartlett J, and Doshi B. *Some patients with cerebral aneurysms are deficient in type III collagen*. The Lancet, 317(8227):973-75, 1981.
5. Baek H, Jayaraman MV, Richardson PD, Karniadakis GE. *Flow instability and wall shear stress variation in intracranial aneurysms*. Journal of The Royal Society Interface, 7(47):967-88, 2010.
6. Cebral JR, Castro MA, Appanaboyina S, Putman CM, Millan D, Frangi AF. *Efficient pipeline for image-based patient-specific analysis of cerebral aneurysm haemodynamics: technique and sensitivity*. IEEE Transactions on Medical Imaging, 24(4):457-67, 2005.

7. Meng H, Wang Z, Hoi Y, Gao L, Metaxa E, Swartz DD, Kolega J. *Complex haemodynamics at the apex of an arterial bifurcation induces vascular remodeling resembling cerebral aneurysm initiation*. Stroke, 38(6):1924-31, 2007.
8. Steinman D, Milner J, Norley C, Lownie S, Holdsworth D. *Image-based computational simulation of flow dynamics in a giant intracranial aneurysm*. American Journal of Neuroradiology, 24:55966, 2003.
9. Imbesi SG, Kerber CW. *Analysis of slipstream flow in a wide-necked basilar artery aneurysm: evaluation of potential treatment regimens*. American Journal of Neuroradiology, 22(4):721-24, 2001.
10. Zeng Z, David FK, Durika M, Ding Y, Lewis DA, Kadirvel R, Robertson AM. *Sensitivity of CFD Based Hemodynamic Results in Rabbit Aneurysm Models to Idealizations in Surrounding Vasculature*. Journal of Biomechanical Engineering, 132(9):091009, 2010.
11. Burleson AC, Strother CM, Turitto VT. *Computer modeling of intracranial saccular and lateral aneurysms for the study of their haemodynamics*. Neurosurgery, 37(4):77484, 1995.
12. Castro MA, Putman CM, Cebral JR. *Patient-specific computational modeling of cerebral aneurysms with multiple avenues of flow from 3D rotational angiography images*. Acad Radiol, 13:81121, 2006.
13. Ford MD, Lee SW, Lownie SP, Holdsworth DW, Steinman DA. *On the effect of parent-aneurysm angle on flow patterns in basilar tip aneurysms: Towards a surrogate geometric marker of intra-aneurismal haemodynamics*. Journal of biomechanics, 41(2):241-48, 2008.
14. Hassan T, Timofeev EV, Saito T, Shimizu H, Ezura M, Matsumoto Y, Takayama K, Tominaga T, Takahashi A. *A proposed parent vessel geometry-based categorization of saccular intracranial aneurysms: computational flow dynamics analysis of the risk factors for lesion rupture*. Journal of neurosurgery, 103(4):662-80, 2005.
15. Kim M, Taulbee DB, Tremmel M, Meng H. *Comparison of two stents in modifying cerebral aneurysm haemodynamics*. Annals of biomedical engineering, 36(5):726-41, 2008.
16. Gambaruto A, Janela J, Moura A, Sequeira A. *Sensitivity of haemodynamics in patient specific cerebral aneurysms to vascular geometry and blood rheology*. Mathematical Biosciences and Engineering, submitted.
17. Gambaruto A, Moura A, Sequeira A. *Topological flow structures and stir mixing for steady flow in a peripheral bypass graft with uncertainty*. Int. J. Numer. Meth. Biomed. Engng., 26:926-53,2010.
18. Lee SW, Steinman DA. *On the relative importance of rheology for image-based CFD models of the carotid bifurcation*. J Biomech Eng. 129:27378, 2007.
19. Venugopal P, Valentino D, Schmitt H, Villablanca JP, Viñuela F, Duckwiler G. *Sensitivity of patient-specific numerical simulation of cerebal aneurysm haemodynamics to inflow boundary conditions*. Journal of neurosurgery, 106(6):1051-60, 2007.
20. Rayz VL, Boussel L, Lawton MT, Acevedo-Bolton G, Ge L, Young WL, Higashida RT, Saloner D. Numerical modeling of the flow in intracranial aneurysms: prediction of regions prone to thrombus formation. Ann Biomed Eng, 36, 1793-1804, 2008.
21. Shojima M, Oshima M, Takagi K, et al. *Role of the bloodstream impacting force and the local pressure elevation in the rupture of cerebral aneurysms*. Stroke, 36:193338, 2005.
22. Cebral JR, Castro MA, Putman CM, Alperin N. *Flow–area relationship in internal carotid and vertebral arteries*. Physiological measurement, 29(5):585-94, 2008.
23. Janela J, Moura A, Sequeira A. *Absorbing boundary conditions for a 3D non-Newtonian fluid-structure interaction model for blood flow in arteries*. International Journal of Engineering Science, 48:1332-49, 2010.
24. Blanco PJ, Pivello MR, Urquiza SA, Feijó RA. *On the potentialities of 3D-1D coupled models in haemodynamics simulations*. Journal of biomechanics, 42(7):919-30, 2009.
25. Formaggia L, Veneziani A. *Reduced and multiscale models for the human cardiovascular system*. Lecture Notes VKI Lecture Series, 7, 2003.
26. Sequeira A, Moura A, Janela J. *Towards a geometrical multiscale approach to non-Newtonian blood flow simulations*. Advances in Mathematical Fluid Mechanics - dedicated to G.P. Galdi on his 60th birthday, 295-309, 2010.
27. Balossino R, Pennati G, Migliavacca F, Formaggia L, Veneziani A, Tuveri M, and Dubini G. *Influence of boundary conditions on fluid dynamics in models of the cardiovascular system: a multiscale approach applied to the carotid bifurcation*. Computer Methods in Biomechanics and Biomedical Engineering, 12(1), 2009.
28. Ho H, Sands G, Schmid H, Mithraratne K, Mallinson G, Hunter P. *A hybrid 1D and 3D approach to haemodynamics modelling for a patient-specific cerebral vasculature and aneurysm*. Medical Image Computing and Computer-Assisted Intervention-MICCAI 2009, 323-30, 2009.
29. Gambaruto AM, Doorly DJ, Yamaguchi T. *Wall Shear Stress and Near-Wall Convective Transport: Comparisons with Vascular Remodelling in a Peripheral Graft Anastomosis*. Journal of Computational Physics. 229(14):5339-5356, 2010.
30. Gambaruto AM, Moura A, Sequeira A. *Topological flow structures and stir mixing for steady flow in a peripheral bypass graft with uncertainty*. International Journal for Numerical Methods in Biomedical Engineering. 26(7): 926-953, 2010.
31. Antiga L, Piccinelli M, Botti L, Ene-Iordache B, Remuzzi A, Steinman DA. *An image-based modeling framework for patient-specific computational haemodynamics*. Med Biol Eng Comput, 46:1097-1112, 2008.
32. Gambaruto AM, Peiró J, Doorly DJ, Radaelli AG. *Reconstruction of shape and its effect on flow in arterial conduits*. Int. J. Numer. Meth. Fluids, 57:495-517,2008.
33. Formaggia L, Moura A, Nobile F. *On the stability of the coupling of 3D and 1D fluid-structure interaction models for blood flow simulations*. Mathematical Modelling and Numerical Analysis, 41(4):743-769, 2007.
34. Hansbo P, Szepessy A. *A velocity-pressure streamline diffusion finite element method for the incompressible Navier-Stokes equations*. Computer methods in applied mechanics and engineering, 84(2):175-192, 1990.